Am J Transl Res 2026;18(2):1455-1472
www.ajtr.org /ISSN:1943-8141/AJTR0169339

Original Article

Efficient differentiation of gonadal somatic cell-like cells (GSCLCs) using magnetic nanoparticles from mouse embryonic stem cells

Ullah Rahman[1*], Zhihui Liu[1,2*], Yuan Gao[1], Xiao Chen[1], Xiaohu Wu[1], Imad Khan[1], Lanjun Liu[3], Fuliang Du[1]

[1]Jiangsu Key Laboratory for Molecular and Medical Biotechnology, College of Life Sciences, Nanjing Normal University, Nanjing 210046, Jiangsu, PR China; [2]Hebei Technology Innovation Center of Cattle and Sheep Embryo, College of Animal Science and Technology, Hebei Agricultural University, Baoding 071000, Hebei, PR China; [3]Chengdu Institute of Biological Products Co., Ltd., 379, 3rd Section, Jinhua Road, Jinjiang District, Chengdu 610023, Sichuan, PR China. [*]Equal contributors.

Received October 15, 2025; Accepted February 9, 2026; Epub February 15, 2026; Published February 28, 2026

Abstract: Objectives: Successful induction of gonadal somatic cell-like cells (GSCLCs) from mouse embryonic stem cells (mES) is important for studying ovarian somatic cell differentiation, development and their function for oocyte genesis and maturation. This study demonstrates the successful differentiation of GSCLCs from mES *in vitro* by utilizing novel green-synthesized Fe_3O_4 nanoparticles (G-Fe_3O_4-NP). Methods: mES were differentiated *in vitro* using G-Fe_3O_4-NP in the absence of BMP4, RA and SHH. GSCLCs identity was confirmed by RT-qPCR analysis of *Foxl2*, *Amh,* and *Gata4,* and by Immunofluorescence staining of FOXL2, AMH, FSHR, and GATA4. Mitochondrial function and cellular redox status were evaluated using JC-1 and DCFH-DA assay. Gene Set Enrichment analysis (GSEA) was performed to evaluate transcriptional reprogramming during GSCLCs differentiation. Results: G-Fe_3O_4-NP derived GSCLCs were achieved without supplementation of BMP4 and retinoic acid considered as key cellular factor for GSCLCs differentiation, suggesting a unique ability of G-Fe_3O_4-NP to independently induce gonadal somatic lineages. Transcriptional profiling and gene set enrichment analysis (GSEA) further elucidated the interplay of transcriptional, epigenetic, and metabolic reprogramming during GSCLC differentiation. Metabolic assessments showed that GSCLCs possessed functional mitochondria and maintain basal oxidative stress levels, reflecting mitochondrial functionality and stability. Key regulators including transcription factor 21 (TCF21), E-cadherin-mediated epithelial stabilization, and interleukin-12 were identified as a critical drivers of GSCLC maturation, supporting cells structural integrity, homeostasis, and gonadal lineage specification. Conclusion: This study establishes that G-Fe_3O_4-NPs enable the cytokine independent derivation of GSCLCs from mES by driving lineage specification. This coordinated transcriptional, epigenetic, and metabolic reprogramming establishes a foundation for in vitro GSCLCs generation.

Keywords: Mouse, embryonic stem cells, gonadal somatic cell-like cells (GSCLCs), magnetic nanoparticles, differentiation *in vitro*, lineage specificity

Introduction

Gonadal somatic cells (GSCs) are essential regulators of follicle oogenesis, coordinating oocytes maturation, steroidogenesis, and follicle development [1, 2]. In mice, interaction between oocytes and surrounding somatic cells began at embryonic days 10 post-coitum (dpc), when primordial germ cells migrated to the genital ridges [3]. During this stage, somatic cells in the genital ridges provides critical signaling cues, such as Fork-head box L2 protein (FOXOL2)/WANT4-centric regulatory gene expression, which promote primordial germ cells (PGC) proliferation while expending themselves to form paired gonads. Following sex determination around embryonic Day 12, somatic cells in female gonads differentiates in to granulosa cells and interstitial cells, which subsequently organized in to ovarian follicle structure [4]. After puberty, primary oocytes resume growth and maturation, a process closely coordinated with ovarian follicle development. These follicles provide structural and functional support essential for oocyte growth and maturation [5, 6]. GSCs maintain germline

https://doi.org/10.62347/ERPS8979

viability through bidirectional communication mediated by growth factors (e.g., growth differentiation factor 9, bone morphogenetic protein 15) and hormonal signals (follicle-stimulating hormone [FSH], anti-Müllerian hormone [AMH] [5, 7].

Despite their critical roles, studies of GSC *in vitro* remain limited by the lack of reliable models that recapitulate their molecular and functional complexity [8]. Primary GSCs rapidly dedifferentiate in culture, losing steroidogenic capacity and marker expression [9]. Recently mouse embryonic stem cells (mES) are used for differentiation into gonadal cell lineages, such as gonadal somatic cell-like cells (GSCLCs) [10, 11] and PGC-like cells. However, only a few papers reported the progress in differentiating pluripotent stem cells into GSCLCs [9, 12], which remains largely challenging. Yoshino et al. (2021) differentiated follicle ovarian somatic cell-like cells (FOSLCs) from mES using defined signaling molecules, such as BMP4, hedgehog (SHH) and retinoic acid (RA) [11]. The gonadal somatic cell lineage-specific fidelity requires precise activation of gene transcriptional networks (e.g., *Foxl2*, GATA binding protein 4 [*Gata4*]) [13, 14] and metabolic adaptations resembling native GSCs [15]. Meanwhile, gonadal cell identity is tightly regulated by epigenetic modifiers (e.g., transcription factor 21 [TCF21]) [16] and adhesion molecules (e.g., E-cadherin [CDH1]) [17], which suppress epithelial-mesenchymal transition and preserve follicular integrity. Additionally, mitochondrial bioenergetics and reactive oxygen species (ROS) homeostasis are critical for GSC function, given that oxidative stress disrupts steroidogenesis and compromises follicle survival [18, 19]. The differentiation of Pluripotent stem cells into GSCLCs remains challenging, relying on complex cytokine combination to activate precise transcriptional and epigenetic programs while maintaining proper metabolic function. This limitation highlights the need of more robust induction platforms [8].

In this context, nanoparticles (NPs) present a promising alternative, as NPs can directly modulate stem cells microenvironments by delivering cues, providing structural scaffolds, and influence key signaling pathways, oxidative stress, and epigenetic states [20, 21]. For example, NP regulate male stem cell differentiation by providing extra-cellular matrix and structural scaffolds mimicking the testis niche and activating SOX9/DMRT1-centric (testis) signal pathway towards sertoli-like cell linage specification [22]. They serve as delivery vehicles for lineage-defining bioactive molecules, such as proteins, miRNA, lipids to targeted cells [23]. In addition, NP can interact with stem cells and influence their behavior, including differentiation, altering gene expression, modulating oxidative stress and affecting cellular microenvironments [21, 24]. Interestingly, Fe_3O_4-NP have also been used to activate the mitogen-activated protein kinase (MAPK) pathway and direct osteogenic differentiation of mesenchymal stem cells with high efficiency [25]. Magnetic nanoparticles (Fe_3O_4-NP) were utilized to precisely modulate cell death signaling pathways *in vitro* and *in vivo* via magnetic field-induced aggregation [26]. In this context, Plants extract-based green synthesized Fe_3O_4-NP offer a distinct advantage, as they exhibit improved biocompatibility compared with chemically synthesized counterparts, primarily due to plant derived phytochemicals that act as natural capping agents and reduced oxidative stress [27]. However, there is no report so far how NP-mediated interaction couples with female FOXL2/WNT4-centric gene transcription regulatory network or ovarian niche factors that determine the fate of GSCLCs during the directed stem cell differentiation.

In this study, we aimed to establish a novel differentiation for generating GSCLCs from mES using green-synthesized magnetic nanoparticles (G-Fe_3O_4-NP). It was reported that Fe_3O_4-NP enhance *Runx2* and *Bmp2* expression during osteogenic differentiation in mouse bone marrow stromal cells [28], which also plays critical roles in gonadal development [29]. We investigated whether G-Fe_3O_4-NP induction can direct mES toward efficient and functional GSCLCs differentiation while preserving cellular integrity, functionality and GSCLCs lineage fidelity. Through comprehensive characterization, including RNA sequencing (RNA-seq), RNA expression assay (*Foxl2*, *Gata4*, *Amh*), protein immunostaining (FOXL2, GATA4, AMH, FSH receptor [FSHR]), and functional assays (5,5',6,6'-tetrachloro-1,1',3,3'-tetraethylbenzimidazolylcarbocyanine iodide [JC-1] for mitochondrial membrane potential; 2',7'-dichlorodihydrofluorescein diacetate [DCFH-DA] for ROS levels), we validated the differentiation efficiency and physiological features of derived GSCLCs

cells. Furthermore, by integrating RNA-seq and gene set enrichment analysis (GSEA), we identified key metabolic pathways (e.g., electron transport chain [ETC], oxidative phosphorylation [OxPhos], tricarboxylic acid [TCA] cycle) and molecular regulators (e.g., TCF21, CDH1, IL-12) governing the process of GSCLCs differentiation. We hypothesized that G-Fe_3O_4-NPs could independently induce gonadal somatic lineage differentiation from mES cells by modulating cellular signaling and epigenetic pathways. This study explored directed ES differentiation into reproductive GSCLCs and elucidated the reprogramming of follicular cell fate and linage specification for the purpose of reconstructing ovarioids to further develop functional oocytes from mES.

Materials and methods

Reagents

All chemicals were purchased from Sigma-Aldrich (St. Louis, MO, USA) unless stated otherwise.

Ethics approval

All animal care and experimental procedures strictly complied with the guidelines of the U.S. National Institutes of Health and were approved by the Institutional Animal Care and Use Committee of Nanjing Normal University (Approval No. IACUC-20201209).

Isolation of Tribulus terrestris extract for G-Fe_3O_4-NP synthesis

Fresh leaves of *T. terrestris* were thoroughly washed with distilled water to remove surface contaminants, air-dried at room temperature (25°C), and ground into a fine powder using a sterile mortar and pestle. For aqueous extract preparation, 10 g of powdered leaves were refluxed in 100 mL of distilled water at 80°C for 30 min under constant stirring. The mixture was then filtered through Whatman No. 1 filter paper to remove particulate matter. The clarified supernatant was cooled to room temperature, aliquoted, and stored at 4°C for subsequent use in nanoparticle synthesis.

Synthesis of G-Fe_3O_4-NP and their characterization

G-Fe_3O_4-NP were synthesized using a green coprecipitation method adapted from Lu et al. (2010) with modifications [30]. Briefly, an aqueous solution containing equimolar concentrations of ferric chloride hexahydrate ($FeCl_3$ $6H_2O$) and ferrous chloride tetrahydrate ($FeCl_2$ H_2O) was prepared by dissolving the sale in 25 mL of deionized water. This solution was mixed with an equal volume (25 mL) of aqueous *T. terrestris* leaf extract at 1:1 (v/v) ratio to coat the nanoparticle. Citric acid was added dropwise as a reducing agent under continuous magnetic stirring (300 rpm) at room temperature for 3 h. After stirring, the reaction mixture was incubated for one additional 1 h to ensure complete precipitation. The resulting magnetic nanoparticles were collected by ultracentrifugation at 13,000 rpm and washed with deionized water to remove unreacted precursors and byproducts. The purified nanoparticles were dried in a convection oven at 80°C for 2 h to yield the final Fe_3O_4 nanoparticle powder.

The crystalline structure of G-Fe_3O_4-NP was analyzed using X-ray Diffraction (XRD) (Rigaku SmartLab, Corporation, Japan) with Cu-Kα radiation (λ = 1.5406 Å) at 40 kV and 30 mA. The diffraction pattern was recorded over a 2θ range of 10°-80° with a step size of 0.02°. Phase identification was performed by matching peaks with the standard JCPDS database (PDF No. 19-0629 for magnetite). The average crystallite size was calculated using the Debye-Scherrer equation. Fourier Transform Infrared Spectroscopy (FTIR) spectra were obtained (PerkinElmer Spectrum 3, USA) in the range of 400-4000 cm^{-1} using the KBr pellet method. Functional groups on the nanoparticle surface were identified based on characteristic absorption bands, including Fe-O vibrations (~580 cm^{-1}) and organic capping agents [31].

mES culture, passage and maintenance

To maintain mES, a 30-mm sterilized culture dish was coated with 1 mL of 0.01% gelatin solution to provide a suitable extracellular matrix for cell attachment. Mitomycin C-treated mouse embryonic fibroblasts (MEF), serving as a feeder layer to support mES growth, were thawed and centrifuged at 1,000 rpm for 5 min to pellet cells and subsequently resuspended in fresh MEF medium (Dulbecco's modified Eagle medium [DMEM] 1X supplemented with 10% fetal bovine serum, 100 U/mL penicillin, and 0.1 mg/mL streptomycin) to ensure cell viability. Resuspended MEFs were plated onto the gelatin-coated dish and allowed to adhere

for a minimum of 6 h at 37°C in a humidified incubator with 5% CO_2. After MEF adherence, the dish was washed with Dulbecco's phosphate-buffered saline (DPBS) to remove non-adherent cells and debris, and was replaced with mES culture medium (2i+LIF) including KnockOut DMEM 1X supplemented with 15% KnockOut Serum Replacement [KSR], 0.3 μM PD0325901 [MAPK/ERK kinase (MEK) 1/2 inhibitor], 3 μM CHIR99021 [glycogen synthase kinase-3 beta inhibitor], 10^3 IU/mL LIF, 2 mM GlutaMAX, 1 mM sodium pyruvate, 50 μM β-mercaptoethanol and 100 U/mL penicillin, 0.1 mg/mL streptomycin. mES were gently dissociated and transferred onto MEF feeder layer coated dish. Fresh 2i+LIF medium was replenished daily to maintain optimal nutrient levels and to support mES growth and self-renewal. mES were cultured for 3d, monitored for growth, and allowed to reach approximately 75% confluency while remaining in pluripotent state prior to GSCLC differentiation.

Induction of epiblast-like cells (EpiLCs)

Pluripotent mES was first induced to epiblast-like celss (EpiLCs) (youshino et al., 2021), and subsequently into GSCLCs. To initiate EpiLCs) differentiation, Matrigel was diluted at a ratio of 1:80 and used to coat a 24 well plate, which was subsequently incubated at 37°C for approximately 1 hour to ensure proper adherence. Passage-5 mES were dissociated by treatment with 1 ml Accutase for 3 mints at 37°C, then neutralized with wash medium (2iLIF) and genital pipetting to achieve a single -cell suspension. Approximately 1 × 10^6 mES were pelleted by centrifugation at 1,200 rpm for 5 min, and subsequently resuspended in 1.5 mL of EpiLC medium (48% v/v DMEM/F12, 48% v/v Neurobasal medium, supplemented with 1% v/v N2 serum-free, 15 μg/mL insulin, 2 mM GlutaMAX, 2% v/v B27 serum-free, 15 ng/mL basic fibroblast growth factor, 20 ng/mL Activin-A, 1 μg/mL G-Fe_3O_4-NP, 100 U/mL penicillin, 0.1 mg/mL streptomycin), and the cell suspension was carefully plated onto the Matrigel-coated wells of the 24-well plate. The plate was incubated at 37°C with 5% CO_2 to promote differentiation, and the medium was replaced with the 1-d to maintain optimal growth conditions. Over the 2-d culture, mES differentiated into EpiLCs under controlled conditions, supported by Matrigel coating and specialized medium.

GSCLC induction and differentiation from EpiLCs

EpiLCs were dissociated with a 3-minutes treatment of 0.05% trypsin at 37°C. The dissociated cells were collected and centrifuged at 1,200 rpm for 5 min, and the pellet resuspended in 2 mL GKF10 medium (80% v/v GMEM, 12% v/v KSR, 3% v/v α-MEM, 3 μM CHIR99021, 10 μM Y27632 [Rho-associated kinase inhibitor], 50 μM β-mercaptoethanol, 1 mM sodium pyruvate, 2 mM GlutaMAX, 1 μg/mL G-Fe_3O_4-NP, 100 U/mL penicillin, 0.1 mg/mL streptomycin). The differentiation process was divided into two phases. In Phase 1 (d1-3), cells were diluted to a concentration of 3 × 10^5 cells/mL in GKF10 medium supplemented with 1 μg/mL G-Fe_3O_4-NP, as dose-response experiments confirmed this concentration to be safe and non-toxic. A 250-μL volume of the cell suspension was plated into each well of a low-attachment 96-well plate and incubated at 37°C; 50 μL of fresh medium was added daily to replenish nutrients and maintain optimal culture conditions. In Phase 2 (d4-6), the medium was completely replaced on d3 with GK10 medium containing 50 ng/mL fibroblast growth factor 9, 1 μg/mL G-Fe_3O_4-NP, and 1 μM PD0325901, but without BMP 4 and/or retinoic acid to support further differentiation and growth. On d5, PD0325901 was withdrawn from the medium. Daily supplementation with 50 μL of fresh medium was continued for next 2d to ensure proper cell growth and development. The differentiation of mES to GSCLCs by BMP4+RA+SHH was done by a previously developed method [11].

Magnetic-activated cell sorting of GSCLCs

GSCLCs were isolated via magnetic-activated cell sorting (MACS) with the Mini-MACS Separation Kit (Miltenyi Biotec, Cat. No. 130-090-312) [11]. Spheroid GSCLCs post differentiation were enzymatically dissociated into individual cells by treatment 0.05% trypsin, to ensure uniform immunolabeling and optimal magnetic separation. The dissociated cells were dual-labeled with magnetic microbead-conjugated anti-stage-specific embryonic antigen-1 (SSEA1) and anti-cluster of differentiation 31 (CD31) antibodies. SSEA1 was used to identify germline precursor cell populations, whereas CD31 enabled further refinement of targeted population [10]. After dual labelling,

the cells were passed through a magnetic column, where SSEA1+/CD31+ positive cells (possibly PGC like cells and/or undifferentiated cells) were retained under the applied magnetic field. In contrast, unlabeled and weakly labeled cells, representing possible GSCLCs population, passed through the column and were finally collected as the GSCLCs targeted fraction. After separation, presumptive GSCLCs were quantified using a hemocytometer to determine their proportion relative to the total cell population.

GSCs from 12.5 dpc mouse gonads were isolated with the similar MACS method and served as controls for GSCLCs.

Dose-dependent cytotoxicity and cell viability assessment of G-Fe_3O_4-NP in GSCLCs and mES using CCK-8 assay

Nanoparticles generate cellular toxicity or niche disruption [32]. To evaluate the biological effects of G-Fe_3O_4-NP, we examined five concentrations (1, 2, 3, 4, and 5 μg/mL). A stable nanoparticle suspension was prepared by dispersing G-Fe_3O_4-NP in GSCLCs and mES culture medium, followed by 30 min of sonication to prevent aggregation. GSCLCs and mES were seeded in 6-well plates and allowed to adhere overnight under standard culture at 37°C, 5% CO_2. After attachment, the medium was replaced with fresh medium containing the respective G-Fe_3O_4-NP concentrations. Respective nanoparticle-free medium was served as control. All treatments were repeated three times for statistical analysis.

Post 72 h of incubation (with medium change every 24 h), cell viability was determined by Cell Counting Kit-8 (CCK-8) assay [33]. Briefly, cells were transferred to a 96-well plate, and CCK-8 reagent was added to each well according to the manufacturer's protocol. After 2-4 h incubation, the absorbance at 450 nm was measured using a microplate reader. The results were normalized to untreated controls to determine relative cell viability at each nanoparticle concentration.

RNA-seq analysis

About 250-300 purified GSCLCs were lysed in 2 μL of lysis buffer (TD503, Vazyme, China), and the extracted RNAs were reverse transcribed into cDNAs via the Single Cell Full-Length mRNA Amplification Kit (N712, Vazyme, China). The cDNA was amplified by PCR to construct sequencing libraries. Library preparation was carried out with the TruePrep DNA Library Prep Kit V2 for Illumina (TD503, Vazyme, China), which utilized a transposase-based tagmentation to fragment and tag the cDNA. The prepared libraries underwent rigorous quality control to assess size distribution, concentration, and integrity before high-throughput sequencing on the NovaSeq 6000 platform. After sequencing, raw reads were processed to remove adapter sequences and filter out low-quality bases. Cleaned reads were aligned to the appropriate reference genome using STAR software, a highly accurate and efficient aligner for RNA-seq data. After alignment, GSEA was performed to identify biologically relevant pathways and gene sets significantly enriched in GSCLCs. The raw sequence data were deposited in the Genome Sequence Archive at the National Genomics Data Center, China National Center for Bioinformation/Beijing Institute of Genomics, Chinese Academy of Sciences (GSA: CRA025129), publicly accessible at https://ngdc.cncb.ac.cn/gs/s/Tyca7tdw.

Reverse transcription and quantitative PCR (RT-qPCR) analysis (RNAs) and immune-fluorescent (IF) staining (proteins)

Relative mRNA expression levels were calculated using an established method [34]. Briefly, total RNA was isolated from MACS (magnetic cells sorted) purified GSCLCs using a triazole-based extraction protocol. cDNA synthesis was performed by adding 5 μL of All-in-One RT MasterMix (Abm, Cat. No. G592 Canada) and incubating the mixture at 25°C for 10 min, 42°C for 30 min, and 85°C for 5 min, respectively, in accordance with the manufacturer's instructions. The *Gapdh* gene was used as an internal control for normalization, and primer sequences are listed in **Table 1**. qPCR was conducted with EvaGreen BlasTaq™ 2X qPCR MasterMix system (Abm, Cat. No. G891, Canada) and the relative mRNA expression level was calculated as described previously [35, 36].

For IF staining, after GSCLCs differentiated at Day 4 (d4) and Day 6 (d6), cells were gently washed three times with PBS, subsequently

Table 1. Primers used for RT-qPCR

Genes	Forward Primer	Reverse Primer	Size bp
AMH	GCTCTGATTCCCGCTGTTTC	CAAGCGAGTGAGGGTCTCTA	183
Gata4	AATCTCCTTCACCCCAGCTC	GAGATGTGCCATGCCTCAAG	189
Foxl2	GTCCGGCATCTACCAGTACA	GGTAGTTGCCCTTCTCGAAC	200
Gapdh	TCAACAGCAACTCCCACTCTTCCA	ACCACCCTGTTGCTGTAGCCGTAT	233

fixation was performed by incubating the cells with 4% paraformaldehyde in PBS for 15 min at room temperature. For permeabilization, the cells were treated with 0.3% Triton X-100 in PBS for 10 min. Nonspecific binding was blocked by incubating with 4% bovine serum albumin for 1 h. Primary antibodies against AMH (Invitrogen, Cat. No. MA5-43969, USA, 1:200 dilution), FOXL2 (Invitrogen, Cat. No. MA5-60883, USA, 1:300 dilution), GATA4 (Invitrogen, Cat. No. MA5-15532, USA, 1:200 dilution), and FSHR (Invitrogen, Cat. No. MA5-61687, USA, 1:300 dilution) were incubated with relative cells overnight at 4°C in a humidified chamber. After PBS washes, fluorophore-conjugated secondary antibody, mouse IgG Alexa Fluor 488 (Invitrogen, Cat. No. A28175, USA, 1:500 dilution) was incubated for 1 h in a light-protected environment. Images were captured using a fluorescence microscope (IX73, Olympus Corporation, Japan).

JC-1 staining (mitochondrial membrane potential [ΔΨm]) for GSCLCs

ΔΨm was evaluated using JC-1 staining [15]. Briefly, a fresh JC-1 dye solution was prepared at a concentration of 2-10 μM in either JC-1 buffer or culture medium. Cells were incubated with the JC-1 solution at 37°C for 30 min at 5% CO_2 in humidified air. After incubation, the cells were washed with warm phosphate-buffered saline (PBS) to remove unbound dye. Stained cells were immediately examined under a fluorescence microscope. In functional and integrated cells, mitochondria emitted red fluorescence due to JC-1 aggregation, whereas depolarized mitochondria exhibited green fluorescence, indicating the presence of monomeric JC-1.

DCFH-DA staining for detecting ROS in GSCLCs

ROS levels were assessed by DCFH-DA staining [37]. Briefly, DCFH-DA was diluted in PBS to a final concentration of 10 μM. Adherent cells were washed once with PBS, then incubated with the DCFH-DA solution for 30 min at 37°C in the dark to allow optimal dye uptake. After incubation, excess dye was removed by washing with PBS. Stained cells were visualized under a fluorescence microscope, detecting green fluorescence at an excitation wavelength of 485 nm and emission wavelength of 535 nm.

Statistical analysis

One-way ANOVA followed by Tukey's HSD test was uesd to evaluate differences in all Immunofluorescence measurements, including FOXL2, AMH, FSHR, GATA4, and H3K37me3, as well as JC-1 and DCFH-DA staining fluorescence intensity among mES cells, GSCLCs induced by G-Fe_3O_4-NP, and GSCLCs induced by BPM4+RA+SHH. RT-qPCR data were analyzed using SPSS 18.0 (IBM, Chicago, IL, USA). Comparisons between two groups were performed using two-tailed Student t-test. Statistically significant was defined as $P < 0.05$.

Results

Structural, chemical and cytotoxic characterization of G-Fe_3O_4-NP nanoparticles

X-ray diffraction analysis confirmed the crystalline structure of synthesized G-Fe_3O_4-NP. The diffraction pattern exhibited characteristic peaks at $2\theta = 35.6°$ and 62.1°, corresponding to the (311) and (440) crystallographic planes of the cubic spinel structure, respectively (**Figure 1A**). These features are consistent with magnetite (Fe_3O_4) phases, and peak broadening reflected the nanoscale dimensions (15-30 nm) of the particles. The overall diffraction pattern identified the dominant cubic spinel phase. Complementary Fourier-transform infrared spectroscopy revealed the chemical composition and surface characteristics of the nanoparticles. The spectrum displayed a strong absorption band at 580 cm^{-1}, corresponding to

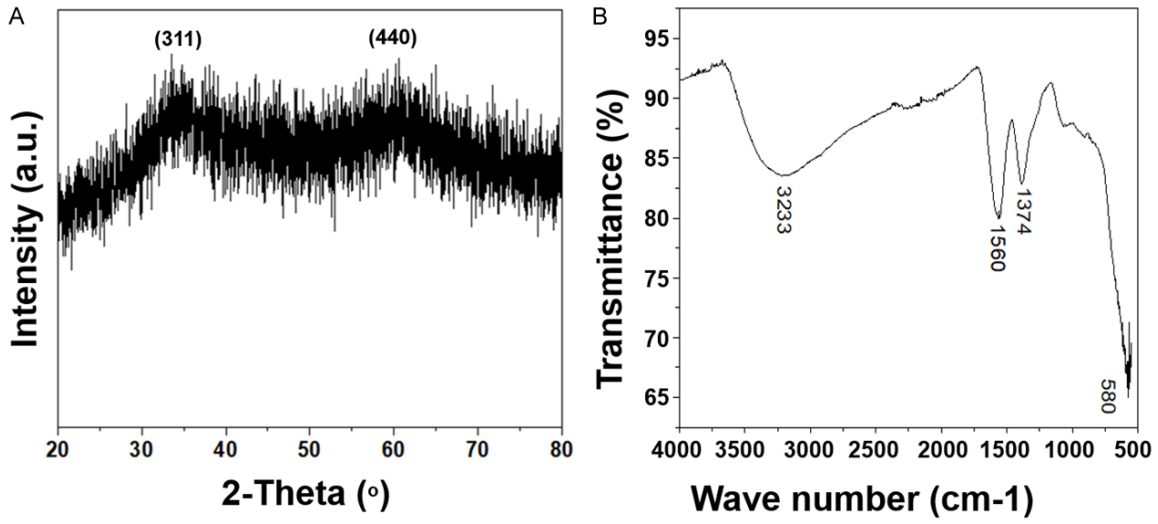

Figure 1. XRD and FTIR analysis of G-Fe_3O_4-NP. A. The XRD pattern exhibited broad peaks at 2θ ≈ 31.1° (311) and 44.0° (400), confirming the nanocrystalline spinel ferrite structure with small crystallite sizes. B. The FTIR spectrum showed characteristic bands at 3233 cm^{-1} (O-H stretch), 1560 and 1374 cm^{-1} (C=O/C-H bends), and 580 cm^{-1} (M-O vibration), confirming metal oxide nanoparticle formation. XRD confirmed the cubic spinel structure of G-Fe_3O_4-NPs (15-30 nm) with peaks at 2θ = 35.6° (311) and 62.1° (440). FTIR revealed Fe-O vibrations (580 cm^{-1}), surface-OH groups (3233 cm^{-1}), adsorbed water (1560 cm^{-1}), and residual nitrates (1374 cm^{-1}).

Fe-O stretching vibration characteristics of both magnetic (Fe_3O_4) and maghemite (γ-Fe_2O_3) spinal structure (**Figure 1B**) additional spectral feature inculed: (1) a broad band at 3233 cm^{-1} attributed to surface hydroxyal (O-H) groups; (2) an broad band at 1560 cm^{-1} arises from physisorbed water molecule (H-O-H bending); and (3) a peak at 1374 cm^{-1} associated with nitrate groups from the green synthesis process.

The does dependent cytotoxicity effect of (G-Fe_3O_4-NP) were quantitatively evaluated using the CCK-8 viability assay. Nanoparticle exposure elicited a concentration-dependent reduction in cells viability over the 72-h treatment period (**Figure 6**). At lowest tested concentration (1 μg/mL), GSCLCs maintained 95.5 ± 2.1% and mES 96 ± 1.5% viability, demonstrating negligible cytotoxicity compered to untreated controls (set as 100%). This non-toxic profile persisted at 2 μg/mL (82.3 ± 1.8% in GSCLCS and 83.7 ± 2.1% in mES viability), suggesting a potential safe threshold below 3 μg/mL. However, a significant ($P < 0.05$) decrease to 70.4 ± 1.2% in GSCLCS and 72.7 ± 1.4% in mES viability emerged at 3 μg/mL, marking the onset of concentration-dependent toxicity. The cytotoxic effects became progressively more pronounced at higher concentrations, with viability declining to 60.1 ± 2.9% in GSCLCS and 63 ± 3.1% in mEs at 4 μg/mL and reaching a minimum of 56.3 ± 2.5% in GSCLCS and 58 ± 3.7% in mEs at the maximum tested dose (5 μg/mL). This monotonic decrease ($R^2 = 0.96$ by linear regression) suggests a strong correlation between nanoparticle concentration and cellular damage. The dosage of 1-2 μg/mL was established as a potential safe working concentration range for subsequent experimental applications of G-Fe_3O_4-NP in this cell system.

Expression of RNAs and proteins of gonadal somatic cell specific genes in GSCLCs by RT-qPCR and IF analysis

To evaluate transcriptional reprogramming during differentiation, the relative mRNA expression profiles of ovarian somatic cell marker genes were analyzed by RT-qPCR. By comparing mES, GSCLCs induced by G-Fe_3O_4-NP and GSCLCs by BMP4+RA method. RT-qPCR analysis revealed significantly and distinctly higher expression patterns among *Foxl2*, *Amh*, and *Gata4* genes in both G-Fe_3O_4-NP and BMP4+RA induced GSCLCs ($P < 0.001$) (**Figure 2**). *Foxl2* was negligibly expressed in mES but showed pronounced upregulation in G-Fe_3O_4-NP and BMP4+RA induced d6 GSCLCs, the fold change was observed round about 37 folds as compared to mES (**Figure 2A**). Similarly, *Amh* was undetectable in mES but exhibited higher expression of 57 folds in d6 G-Fe_3O_4-NP and

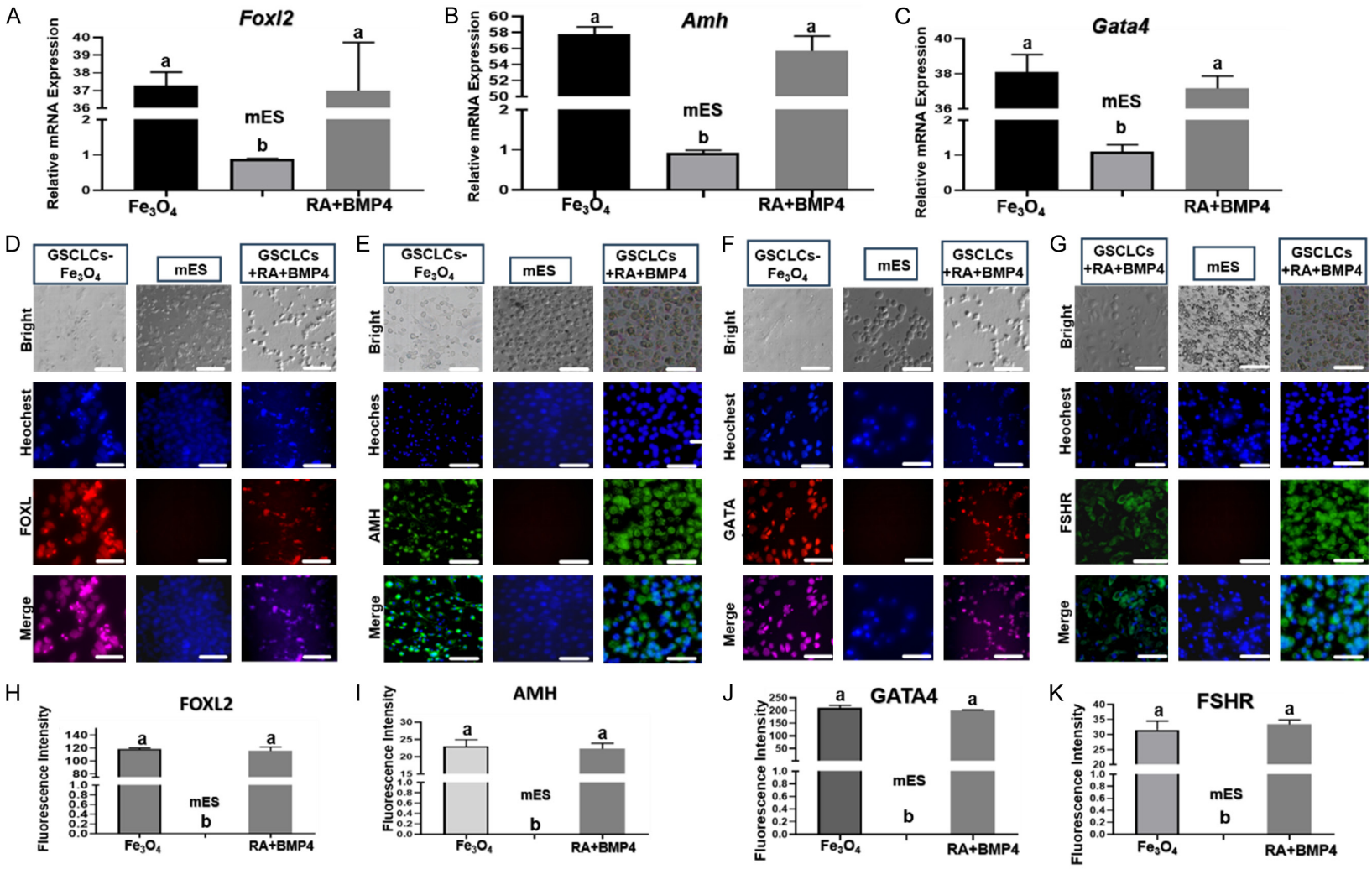

Figure 2. Characterization of GSCLCs and ESCs by immunofluorescence staining and mRNA analysis. A. Relative mRNA expression of *Foxl2*, a transcription factor essential for gonadal cell development, in ESCs and GSCLCs. B. Relative mRNA expression of *Amh*, a marker associated with gonadal cell differentiation and function, in ESCs and GSCLCs. C. Relative mRNA expression of *Gata4*. D. Fluorescence analysis of FOXL2 expression in GSCLCs induced with or without Fe_3O_4 than in mES, with phase contrast, blue signals of Hochest, Red signals of FOXL2 and Merge image. E. Fluorescence microscopy analysis of AMH expression both in mES and GSCLCs induced with or without Fe_3O_4. The imaging included phase contrast, Hoechst staining (blue) for nuclei localization, and specific green fluorescence signals corresponding to AMH protein expression. A merged image combination of all channels for comparative analysis. F. Fluorescence analysis of GATA4 expression in both GSCLCs induced by either Fe_3O_4 or BPM4+RA as well as in mES was performed using phase contrast microscopy, along with blue Hoechst staining to

identify nuclei and red fluorescence signals to detect GATA4 protein expression. G. Fluorescence microscopy analysis of FSHR expression both in mES and GSCLCs. The imaging included phase contrast, Hoechst 33342 staining blue, and specific green fluorescence signals corresponding to FSHR protein expression. H-K. These figures are the fluorescence intensity analysis of FOXL2, AMH, GATA4 and FSHR respectively. Images are representative of three independent experiments. Note the distinct expression patterns of somatic cell markers (FOXL2, AMH, GATA4, FSHR) in d6 GSCLCs induced by either Fe_3O_4 or BPM4+RA relative to ESCs both in Immunofluorescence staining and mRNA analysis, indicating progressive acquisition of GSC characteristics during differentiation. Scale bars: 100 μm.

BMP4+RA induced GSCLCs (**Figure 2B**). *Gata4* displayed 38 folds higher expression in d6 G-Fe_3O_4-NP and BMP4+RA induced GSCLCs (**Figure 2C**).

Immunofluorescence (IF) analysis further validated the successful differentiation of GSCLCs from mES, as indicated by the expression of key gonadal lineage markers. GSCLCs (d6) exibhited distinct epithelial morphology in brightfield images. Critical makers of GSC identity were highly expressed in both G-Fe_3O_4-NP and BMP4+RA induced GSCLCs but absent in mES. FOXL2 expression was significantly upregulated, showing an approximately 120-fold increase in GSCLCs induced by either method, while it remained undetectable in undifferentiated mES cells (**Figure 2D**). AMH, exhibited cytoplasmic and perinuclear localization in GSCLCs, Quantitative analysis revealed an approximate 23-fold increase of AMH in GSCLCs generated via either method, contrasting with its complete absence in undifferentiated mES control (**Figure 2E**). GATA4, showed prominent nuclear expression in GSCLCs, GATA4 expression was markedly upregulated in GSCLCs generated by both induction method, exhibiting an approximately 200-fold increase as compared to undifferentiated mES (**Figure 2F**). FSHR exhibited clear membrane-associated staining in GSCLCs, and showed in approximately 32-fold increase as compared to undifferentiated mES (**Figure 2G**). The expression patterns of FOXL2, GATA4 and the spatial overlap of FSHR and AMH with nuclear DNA reinforced the ovarian gonadal somatic cell-like identity of the differentiated population. IF intensity analysis indicated significantly higher expression of gonadal somatic cell markers as FOXL2 (**Figure 2H**), AMH (**Figure 2I**), GATA4 (**Figure 2J**) and FSHR (**Figure 2K**) in GSCLCs than that in mES ($P < 0.05$).

Dynamic remodeling of H3K27me3 during GSCLC differentiation

Immunofluorescence (IF) analysis indicated a dynamic increase of H3K27me3 modification during progressive six days of GSCLCs differentiation from mES. It was observed that D6 GSCLCs and 12.5 dpc GSC exhibited approximately three-fold higher H3K37me3 signal intensity compared to d4 GSCLCs and mES cells (**Figure 3**). On d4 differentiation, GSCLCs displayed intermediate H3K27me3 signal higher than that in mES ($P < 0.05$) (**Figure 3A**). GSCLCs on d6 exhibited the strongest H3K27me3 signals with widespread nuclear deposition, significantly exceeding the levels of d4 GSCLCs ($P < 0.05$) and mEs ($P < 0.05$), respectively, but closely approximated those in mature 12.5 dpc GSCs (**Figure 3B**).

Mitochondrial functional analysis and oxidative stress status of GSCLCs

To assess the metabolic integrity of GSCLCs, mitochondrial membrane potential (ΔΨm) and intracellular Reactive Oxygen species (ROS) levels were evaluated via JC-1 and DCFH-DA staining, respectively (**Figure 4**). JC-1 analysis revealed prominent red fluorescence (aggregate form) in GSCLCs, indicative of preserved ΔΨm and functional mitochondria. Corresponding green fluorescence (monomeric form) remained at baseline levels. Merged images showed a high red-to-green fluorescence ratio (**Figure 4A**), confirming normal mitochondrial polarization in most cells. JC-1 fluorescence intensity analysis showed that similar mitochondrial membrane potential (ΔΨm) between G-Fe_3O_4-NP GSCLCs and d12.5 Gonad GSC, indicating comparable mitochondrial activity (**Figure 4B**).

Parallel analysis of oxidative stress status using DCFH-DA staining found a minimal green fluorescence in most GSCLCs, indicating maintenance of basal ROS levels. (**Figure 4C**). DCFH-DA fluorescence intensity analysis indicated non-significant difference in intracellular ROS levels between G-Fe_3O_4-NP GSCLCs and controls (d12.5 Gonad GSC) (**Figure 4D**) ($P > 0.05$), suggesting that G-Fe_3O_4-NP exposure did not induce oxidative stress under the tested conditions.

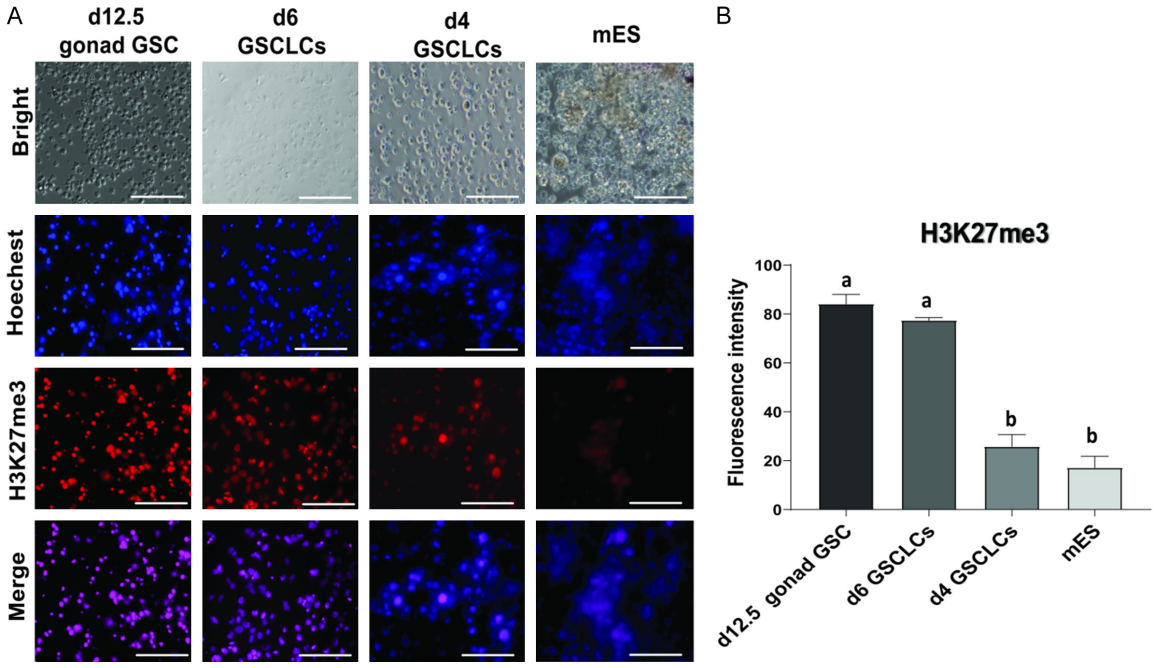

Figure 3. Assessment of H3K27me3 expression during GSCLCs differentiation. A. Fluorescence microscopy analysis of H3K27me3 in 12.5 dpc gonadal somatic cells from mice, d6 GSCLCs, d4 GSCLCs and mES. Hoechst 33342 image is for nuclei and a merged image combination of all channels for comparative analysis. B. Fluorescence intensity analysis of H3K27me3 in 12.5 dpc gonadal somatic cells from mice, d6 GSCLCs, d4 GSCLCs and mES. Images are representative of ≥ 3 independent experiments. Progressive H3K27me3 accumulation from ESCs to d4 GSCLCs to d6 GSCLCs reflects stage-specific chromatin remodeling during germ cell-like differentiation. Notably, d6 GSCLCs exhibit the strongest H3K27me3 signal, consistent with their terminally differentiated state. Scale bars: 100 μm.

Transcriptional and epigenetic orchestration in GSCLC differentiation on d6

To elucidate the dynamic interplay of transcriptional and epigenetic mechanisms governing GSCLCs differentiation, we performed Gene Set Enrichment Analysis (GSEA) comparing the transcriptional profiles of d6 GSCLCs and d4 GSCLCs (**Figure 5**). This analysis indicated a marked activation of mitochondrial metabolic pathways, intercellular adhesion, and immune modulation, reflecting a coordinated ontological transition toward GSC-like lineage specification. Quantitative analysis showed significant differences in metabolic pathway activation (normalized enrichment scor [NES] > 2, P < 0.001) between d4 and d6 GSCLCs. The ETC (**Figure 5A**) and TCA cycle, respiratory electron transport pathway (**Figure 5B**) showed an NES > 2.000, OxPhos pathway exhibited an NES > 2.226, indicating substantial upregulation by d6 then d4 (**Figure 5C**), suggesting enhanced mitochondrial respiration and energy production as differentiation progressed. Similarly, Voxphos pathway, with an NES > 2.244 (**Figure 5D**), and mitochondrial-associated genes pathway, represented by an NES > 1.583 (**Figure 5E**) of d6 GSCLCs as compared to d4 counterpart, which indicated an improved mitochondrial integrity and metabolic function in d6 GSCLCs. The ribosome genes show strong enrichment (NES > 2.205, P < 0.001) in the d6 GSCLCs, indicating upregulating ribosomal activity (**Figure 5F**). Furthermore, TCF21 displayed moderate but significant upregulation of its genes (NES > 1.555, P < 0.001; **Figure 5G**). Enrichment of CDH1 associated-pathway (NES > 1.819, P < 0.003; **Figure 5H**) underscore a paradigm shift toward epithelial stabilization. Similarly, IL-12 showed dramatic enrichment (NES > 1.685, P < 0.005; **Figure 5I**), which this immunological priming may help to maintain cellular homeostasis during differentiation.

Discussion

We clearly demonstrated that a novel G-Fe_3O_4-NP induction can efficiently promote lineage-specific GSCLCs differentiation from pluripotent mES. In our study, G-Fe_3O_4-NP derived

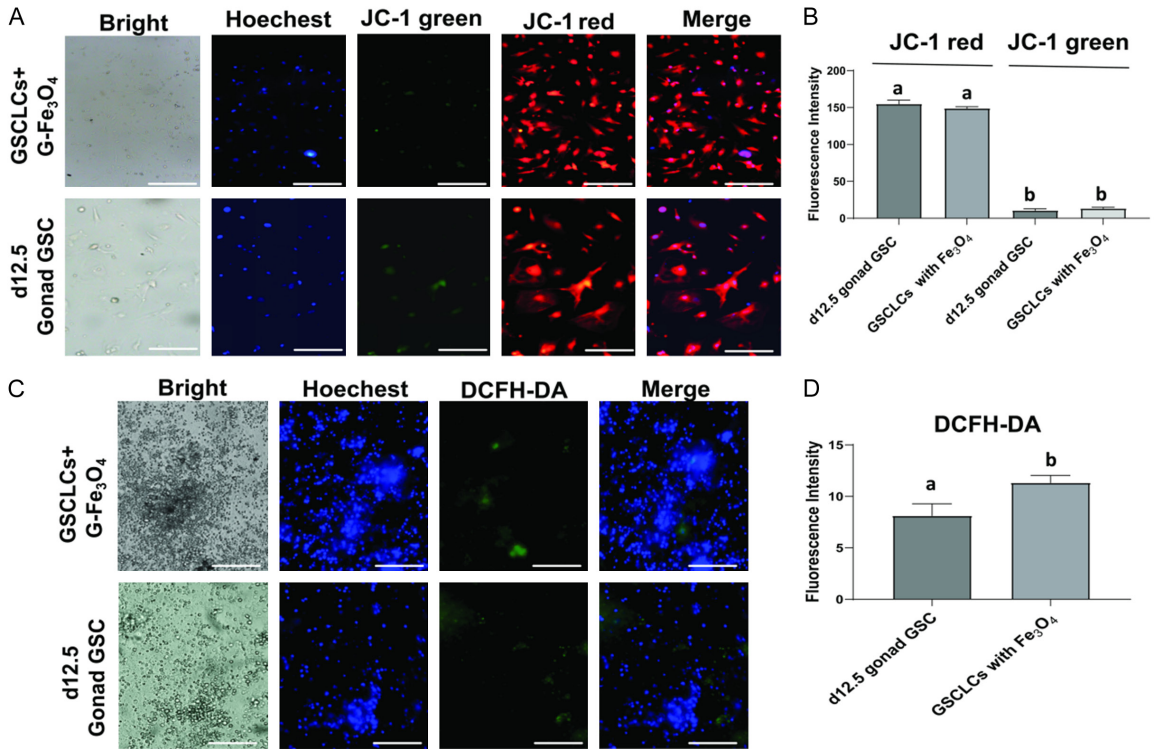

Figure 4. Assessment of ΔΨm and ROS levels in GSCLCs. A. ΔΨm using JC-1 staining of GSCLCs with G-Fe_3O_4-NP treatment and d12.5 Gonad GSC. Green fluorescence indicates depolarized mitochondria, while red fluorescence represents polarized mitochondria. Nuclei were counterstained with Hoechst 33342 (blue). B. Fluorescence intensity analysis for JC-1 staining of GSCLCs with G-Fe_3O_4-NP treatment and d12.5 Gonad GSC. C. The DCFH-DA staining of GSCLCs with G-Fe_3O_4-NP treatment and d12.5 Gonad GSC for ROS analysis. D. Fluorescence intensity analysis of DCFH-DA staining. These findings provide insights into the functional status of mitochondria and the oxidative stress environment in GSCLCs, highlighting their metabolic activity and redox homeostasis. Scale bars: 100 μm.

GSCLCs represented a wide range of GCS specific cell lineage gene markers including *Foxl2*, *Amh* and *Gata4*, which showed a significant increase in their expression as compared to pluripotent mES. Our Immunofluorescence (IF) analysis further conformed the positive protein expression of FSHR, FOXL2, AMH and GATA4 in mES derived GSCLCs. In fact, substantial upregulation of these genes in GSCLCs highlights the transcriptional reprogramming required for GSC specification [37]. The colocalization of FSHR and AMH, along with the co-expression of FOXL2 and GATA4, strongly supports the acquisition of a granulosa cell-like phenotype and broader GSC characteristic [38-40]. These GSC specific genes play pivotal role in follicular development, oocyte support, and steriodogenesis [41]. *Fshr* mediates FSH-driven follicle growth and estrogen synthesis, whereas AMH inhibits excessive follicle activation to preserve the ovarian reserve [42]. In mouse, *Amh* gene critical for Müllerian duct regression and granulosa cell's function plays role in this GSC differentiation [43]. *Foxl2* maintains granulosa cell identity, and *Gata4* regulates steroidogenic genes essential for ovarian function and fertility [44]. It was reported that loss of *Foxl2* results in ovary-to-testis sex reversal in fish and goats, as well as postnatal sex reversal in mice [45]. The role of *Foxl2* gene in driving ovarian-like cell fate specification during differentiation reinforces its important role in establishing somatic cell identity in GSCLCs and its involvement in GSC lineage commitment [38]. A recent study reported that *Foxl2* gene in humans appears to direct differentiating cells by establishing a transitional identity prior to committing the early gonadal support cell fate [46]. *Gata4* was also significantly expressed in differentiated GSCLCs (**Figure 2A**), highlighting the functional maturation of these cells toward a GSC identity [47]. In goat ovaries, *Gata4* showed a stronger expression in granulosa cells (GCs) [44]. Our findings provide molecular

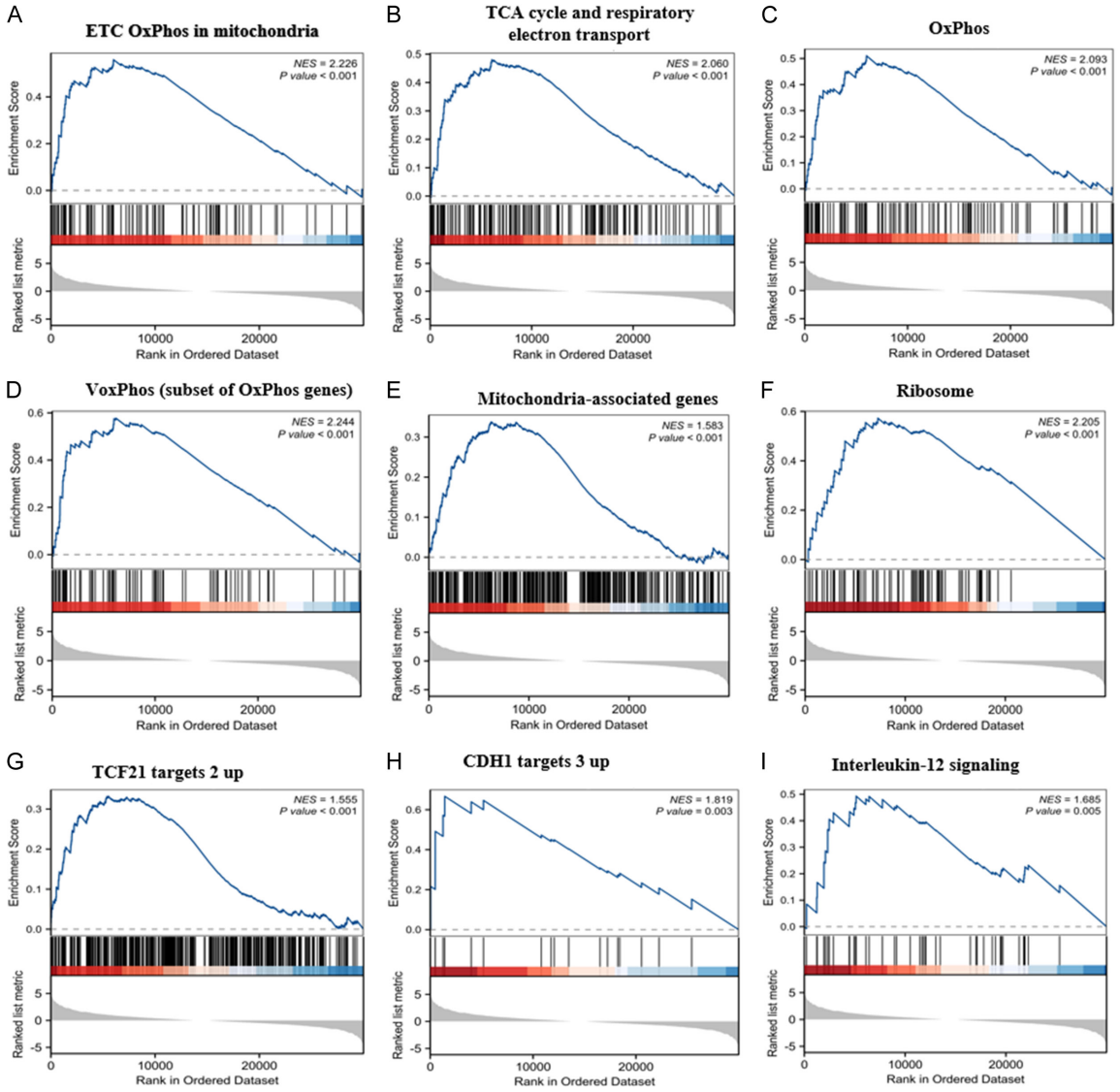

Figure 5. GSEA of mitochondrial and OxPhos pathway, as well as regulators TCF21, CDH1, and IL-12. Enrichment plots illustrate the enrichment scores (y-axis) across ranked gene lists (X-axis), showing the distribution of gene set associated with mitochondrial function and OxPhos. The normalized enrichment score (NES) and *p*-velues indicate significant enrichment in the analyzed dataset. A. ETC and OxPhos system in mitochondria (NES = 2.226, $P < 0.001$). B. TCA cycle and respiratory electron transport (NES = 2.060, $P < 0.001$). C. OxPhos (NES = 2.093, $P < 0.001$). D. Voxphos, a subset of OxPhos genes (NES = 2.244, $P < 0.001$). E. Mitochondria-associated genes (NES = 1.583, $P < 0.001$). F. Ribosome-related genes (NES = 2.205, $P < 0.001$). G. GSEA plot for "TCF21 targets 2 up". The NES is 1.555, with a sarcastically significant *p*-value ($P < 0.001$). The enrichment scor cure peak early in the ranked dataset, indicating strong positive enrichment of this gene set. H. GSEA plot for "CHD1 target 3 up" The NES is 1.819, with a *p*-value $P < 0.003$, denoting significant enrichment of this gene set. The cure demonstrated the positive enrichment near the top of ranked dataset. I. GSEA plot for "Interleukin-12". The NES is 1.885, with a *p*-value $P < 0.005$, confirming significant pathway enrichment. The black vertical bars represent gene hits with in the ranked dataset, with the enrichment signal reflected in the upward peak of the enrichment score. The color gradient (red to blue) represents ranking correlation. High NES values suggest strong associations of these pathways with the analyzed condition.

evidence of successful differentiation and align with the established roles of *Foxl2*, *Amh*, and *Gata4* genes in mouse gonadal development and function. In addition, H3K27me3 epigenetic modification revealed a progressive increase in expression during GSCLCs differentiation from mES. The dynamic H3K27me3 signature pattern was similar to that of mouse *in vivo* GSC

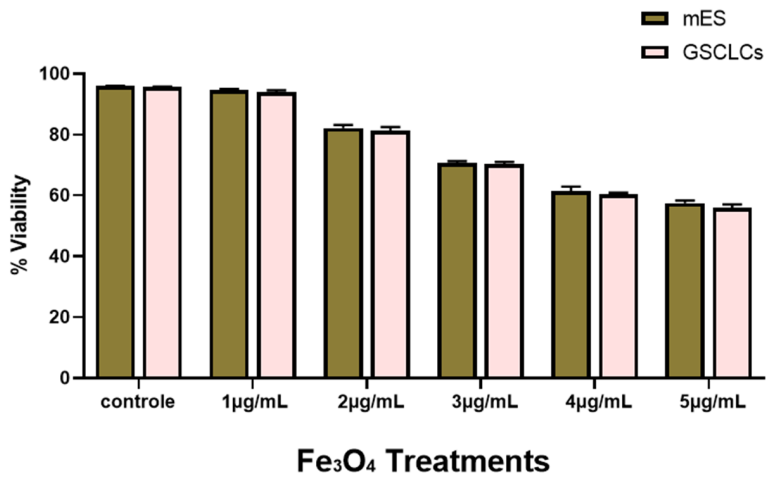

Figure 6. Dose-dependent effects of G-Fe_3O_4-NP on cells viability. Cells viability (%) of mES and GSCLCs following exposure to increasing concentration of G-Fe_3O_4-NP (control, 1, 2, 3, 4 and 5 μg/mL). Both cells' types exhibited a gradual, concentration dependent decline in viability with increasing G-Fe_3O_4-NP doses. Data are presented as mean ± standard deviation (SD), indicating comparable sensitivity patterns between mES and GSCLCs across the tested concentrations range.

cells (**Figure 3**). It was reported that modification of H3K27me2/me3 via genome editing alters ESC differentiation trajectories and destabilizes the ground-state pluripotency network [48]. Recently, we have successfully reconstructed mouse ovarioids with follicular structures by those G-Fe_3O_4-NP derived GSCLCs and PGCLCs from mES (Du et al., unpublished data). Taken together, our study with G-Fe_3O_4-NP established GSCLCs as a reliable model for studying gonadal cell biology and associated reproductive approach to differentiate functional oocytes from mES [49].

Gene Set Enrichment Analysis (GSEA) revealed the dynamic interplay of transcriptional and epigenetic mechanisms regulating GSCLC differentiation. In d6 GSCLCs, mitochondrial pathways associated with the electron transport chain (ETC), Oxidative phosphorylation (OxPhos), and TCA cycle were upregulated, indicating enhanced mitochondrial respiration and energy production during differentiation (**Figure 5**). The metabolic profile of stem cells typically shifts from glycolysis to mitochondrial OxPhos during cell differentiation, accompanied by dynamic changes in mitochondrial morphology and higher ATP yield [39, 50]. This metabolic transition aligns with the increased energy demands of differentiated cells and indicates the importance of mitochondrial integrity in supporting cellular function [51]. The activation of CDH1 highlights the role of epithelial stabilization and intercellular cohesion in maintaining structural fidelity during lineage commitment [52]. The enrichment of IL-12 signaling also indicates a potential role in immune modulation and microenvironmental adaptation, supporting cellular homeostasis during differentiation [53, 54]. Collectively, these key processes can act accordingly to direct GSCLCs differentiation. Oxidative phosphorylation pathway supports stem cell differentiation [55]. Through ATP generation to meet high energy demands of germ cell development, coupled with broader metabolic reprogramming, cellular metabolism plays an important role capable of directing lineage-specific differentiation [40, 56]. TCF21 reprograms genetic activity, likely fine-tuning cellular identity and stress responses as Shen et al. reported $TCF21^{lin}$ cells act as bipotential somatic progenitors in the ovary and testis, and additionally serve as reserve progenitors for tissue maintenance and repair [55, 57]. By d6 GSCLCs induction, the dynamic GSEA model coordinated genetic reprogramming, structural reinforcement, metabolic transition and immune signaling which had driven the induced cells toward a specialized GSC-like identity, and met with physical and metabolic demands for cell differentiation [58].

Mitochondrial membrane potential (ΔΨm) and intracellular Reactive oxygen species (ROS) levels serve as critical indicators for cellular functionality [59]. The decrease in ΔΨm relative to normal levels may compromise cell viability [60]. ΔΨm measurements in our study revealed a prominent red JC-1 Fluorescence in G-Fe_3O_4-NP induced GSCLCs compered to control (**Figure 3**), indicating that a high level of ΔΨm in GSCLCs with intracellular metabolically active and functional mitochondria. The low intracellular ROS levels observed in our study further supported metabolic stability with a balance redox state conducive to cellular homeostasis.

Intracellular ROS levels function not only as a cornerstone of bioenergetics but as a key regulator of diverse cellular processes, including ion transport, and redox signaling [61-63]. Our finding supports that GSCLCs are functional and capable of meeting the high energy demands of proliferative and functionally active cells [64, 65].

Our novel G-Fe_3O_4-NP directed GSCLCs differentiation achieved over 78% GSCLCs within a very shorter time-frame compared to existing protocols which typically achieve 55-60% of GSCLC efficiency (Wang et al., 2021; Yoshino et al., 2021). Notably, our approach performed GSCLCs induction without addition of BMP, SHH and RA and other small inducing molecules [10, 11]. Yoshino et al demonstrated the derivation of follicle ovarian somatic cell-like cells (FOSLCs) from mES using defined signaling molecules, BMP4, SHH, RA, and fibroblast growth factor 9 (FGF9) [11], while Wang et al derived GSCLCs from mES with two small molecules: vitamin C (ascorbic acid) and the retinoid receptor agonist AM580 [66]. The biological mechanisms of G-Fe_3O_4-NP for activating signal pathways during GSCLCs differentiation still require a further investigation. This study is limited by the use of a single cell line and in-vitro differentiation system without in-vivo validation. Further work is needed to confirm the signaling pathways underlying nanoparticle-mediated induction. A recent study found that incorporating Fe_3O_4-CA-NPs into VDF-TrFE polymer scaffolds enhances key cellular signaling pathways, including BMP, TGF-β, and Wnt [66, 67]. The effects of G-Fe_3O_4-NP nanoparticles on GSCLCs differentiation may be mediated, in part, by modulation of key transcription regulators, including runt-related transcription factor 2 (*Runx2*), BMP, TGF-β, and Wnt. Previous studies indicated that Fe_3O_4 nanoparticles enhance the expression of *Runx2* and BMP, TGF-β, and Wnt during osteogenic differentiation of mouse bone marrow stromal cells [29, 68-70]. These factors also play critical roles in gonadal cell development that *Runx2* and *Bmp2* were essential for GSC differentiation and function [71, 72]. Sun et al., identified the MAPK cascade as a critical regulator of cell differentiation in according to that Fe_3O_4 nanoparticles can activate the MAPK signaling pathway [26, 73]. Studies show that Fe_3O_4 nanoparticles generate a micro-magnetic field which can stimulate cell growth and proliferation [67, 68], which affects protein crystallization, integrin and extracellular matrix protein binding, and cell adhesion [71]. It was reported that Fe_3O_4 nanoparticles can directly activate calcium ion (Ca^{2+}) channels that drive various signaling pathways, such as MAPK and BMP [55, 72]. We also hypothesize that there are a small trace of ligands existing in culture medium or secreted by induced cells while G-Fe_3O_4-NP can amplify their effects during signal transduction pathways. Further investigation is warranted to explore inherent cellular and biological mechanisms of G-Fe_3O_4-NP during germ cell related differentiation.

In conclusion, our study demonstrated the novel and efficient generation of GSCLCs by differentiating mES with G-Fe_3O_4 nanoparticles, but without exogenous BMP4, sonic hedgehog (SHH) and retinoic acid (RA). The mES derived GSCLCs recapitulated GSC specific molecular, functional and metabolic characteristics. This work exploits the understanding of gonadal somatic cell differentiation and development for future generating functional follicles and oocytes from stem cells in animal reproduction, breeding and human reproductive medicine.

Acknowledgements

This study was supported in part by National Natural Science Foundation of China (Grant Nos. 32372877, 31872353, and 32072732). The authors thank BioScience Writers, LLC, for scientific editing support.

Disclosure of conflict of interest

None.

Abbreviations

mES, mouse embryonic stem cells; EpiLCs, epiblast-like cells; GSCLCs, gonadal somatic cell-like cells; MEFs, mouse embryonic fibroblasts; H3K27me3, trimethylation of histone H3 at lysine 27; G-Fe_3O_4-NPs, Green synthesized iron oxides nanoparticle.

Address correspondence to: Dr. Fuliang Du, Jiangsu Key Laboratory for Molecular and Medical Biotechnology, College of Life Sciences, Nanjing Normal University, #1 Wenyuan Road, Nanjing 210046, Jiangsu, PR China. Tel: +86-25-85898011;

E-mail: fuliangd@njnu.edu.cn; Lanjun Liu, Recombinant Protein Drugs and Novel Vaccine Research Lab, Chengdu Institute of Biological Products Co. Ltd., #379, Section 3, Jinhua Road, Chengdu 610023, Sichuan, PR China. Tel: +86-28-84418232; E-mail: liulanjun@sinopharm.com

References

[1] Binelli M and Murphy BD. Coordinated regulation of follicle development by germ and somatic cells. Reprod Fertil Dev 2010; 22: 1-12.

[2] Stévant I, Kühne F, Greenfield A, Chaboissier MC, Dermitzakis ET and Nef S. Dissecting cell lineage specification and sex fate determination in gonadal somatic cells using single-cell transcriptomics. Cell Rep 2019; 26: 3272-3283, e3.

[3] Hikabe O, Hamazaki N, Nagamatsu G, Obata Y, Hirao Y, Hamada N, Shimamoto S, Imamura T, Nakashima K, Saitou M and Hayashi K. Reconstitution in vitro of the entire cycle of the mouse female germ line. Nature 2016; 539: 299-303.

[4] Hayashi K, Ohta H, Kurimoto K, Aramaki S and Saitou M. Reconstitution of the mouse germ cell specification pathway in culture by pluripotent stem cells. Cell 2011; 146: 519-532.

[5] Monniaux D. Driving folliculogenesis by the oocyte-somatic cell dialog: lessons from genetic models. Theriogenology 2016; 86: 41-53.

[6] Mork L, Maatouk DM, McMahon JA, Guo JJ, Zhang P, McMahon AP and Capel B. Temporal differences in granulosa cell specification in the ovary reflect distinct follicle fates in mice. Biol Reprod 2012; 86: 37.

[7] Garcia-Alonso L, Lorenzi V, Mazzeo CI, Alves-Lopes JP, Roberts K, Sancho-Serra C, Engelbert J, Marečková M, Gruhn WH, Botting RA, Li T, Crespo B, van Dongen S, Kiselev VY, Prigmore E, Herbert M, Moffett A, Chédotal A, Bayraktar OA, Surani A, Haniffa M and Vento-Tormo R. Single-cell roadmap of human gonadal development. Nature 2022; 607: 540-547.

[8] Gonen N, Eozenou C, Mitter R, Elzaiat M, Stévant I, Aviram R, Bernardo AS, Chervova A, Wankanit S, Frachon E, Commère PH, Brailly-Tabard S, Valon L, Barrio Cano L, Levayer R, Mazen I, Gobaa S, Smith JC, McElreavey K, Lovell-Badge R and Bashamboo A. In vitro cellular reprogramming to model gonad development and its disorders. Sci Adv 2023; 9: eabn9793.

[9] Britt KL, Stanton PG, Misso M, Simpson ER and Findlay JK. The effects of estrogen on the expression of genes underlying the differentiation of somatic cells in the murine gonad. Endocrinology 2004; 145: 3950-3960.

[10] Wang H, Liu L, Liu C, Wang L, Chen J, Wang H, Heng D, Zeng M, Liu C, Zhou Z, Ye X, Wan Y, Li H and Liu L. Induction of meiosis by embryonic gonadal somatic cells differentiated from pluripotent stem cells. Stem Cell Res Ther 2021; 12: 607.

[11] Yoshino T, Suzuki T, Nagamatsu G, Yabukami H, Ikegaya M, Kishima M, Kita H, Imamura T, Nakashima K, Nishinakamura R, Tachibana M, Inoue M, Shima Y, Morohashi KI and Hayashi K. Generation of ovarian follicles from mouse pluripotent stem cells. Science 2021; 373: eabe0237.

[12] Romualdez-Tan MV. Modelling in vitro gametogenesis using induced pluripotent stem cells: a review. Cell Regen 2023; 12: 33.

[13] Uhlenhaut NH, Jakob S, Anlag K, Eisenberger T, Sekido R, Kress J, Treier AC, Klugmann C, Klasen C, Holter NI, Riethmacher D, Schütz G, Cooney AJ, Lovell-Badge R and Treier M. Somatic sex reprogramming of adult ovaries to testes by FOXL2 ablation. Cell 2009; 139: 1130-1142.

[14] Rojas A, De Val S, Heidt AB, Xu SM, Bristow J and Black BL. Gata4 expression in lateral mesoderm is downstream of BMP4 and is activated directly by Forkhead and GATA transcription factors through a distal enhancer element. Development 2005; 132: 3405-3417.

[15] Mandal S, Lindgren AG, Srivastava AS, Clark AT and Banerjee U. Mitochondrial function controls proliferation and early differentiation potential of embryonic stem cells. Stem Cells 2011; 29: 486-495.

[16] Tamura M, Kanno Y, Chuma S, Saito T and Nakatsuji N. Pod-1/Capsulin shows a sex- and stage-dependent expression pattern in the mouse gonad development and represses expression of Ad4BP/SF-1. Mech Dev 2001; 102: 135-144.

[17] Piprek RP, Kloc M, Mizia P and Kubiak JZ. The central role of cadherins in gonad development, reproduction, and fertility. Int J Mol Sci 2020; 21: 8264.

[18] Kobayashi H, Yoshimoto C, Matsubara S, Shigetomi H and Imanaka S. Altered energy metabolism, mitochondrial dysfunction, and redox imbalance influencing reproductive performance in granulosa cells and oocyte during aging. Reprod Sci 2024; 31: 906-916.

[19] Devine PJ, Perreault SD and Luderer U. Roles of reactive oxygen species and antioxidants in ovarian toxicity. Biol Reprod 2012; 86: 27.

[20] Wei M, Li S and Le W. Nanomaterials modulate stem cell differentiation: biological interaction and underlying mechanisms. J Nanobiotechnology 2017; 15: 75.

[21] Pan Y, Du X, Zhao F and Xu B. Magnetic nanoparticles for the manipulation of proteins

and cells. Chem Soc Rev 2012; 41: 2912-2942.
[22] Shams A, Eslahi N, Movahedin M, Izadyar F, Asgari H and Koruji M. Future of spermatogonial stem cell culture: application of nanofiber scaffolds. Curr Stem Cell Res Ther 2017; 12: 544-553.
[23] Ramírez-Cando LJ, De Simone U and Coccini T. Toxicity evaluation of iron oxide (Fe3O4) nanoparticles on human neuroblastoma-derived SH-SY5Y cell line. J Nanosci Nanotechnol 2017; 17: 203-211.
[24] Abdal Dayem A, Lee SB and Cho SG. The impact of metallic nanoparticles on stem cell proliferation and differentiation. Nanomaterials (Basel) 2018; 8: 761.
[25] Wang Q, Chen B, Cao M, Sun J, Wu H, Zhao P, Xing J, Yang Y, Zhang X, Ji M and Gu N. Response of MAPK pathway to iron oxide nanoparticles in vitro treatment promotes osteogenic differentiation of hBMSCs. Biomaterials 2016; 86: 11-20.
[26] Cho MH, Lee EJ, Son M, Lee JH, Yoo D, Kim JW, Park SW, Shin JS and Cheon J. A magnetic switch for the control of cell death signalling in in vitro and in vivo systems. Nat Mater 2012; 11: 1038-1043.
[27] Dowlath MJH, Musthafa SA, Mohamed Khalith SB, Varjani S, Karuppannan SK, Ramanujam GM, Arunachalam AM, Arunachalam KD, Chandrasekaran M, Chang SW, Chung WJ and Ravindran B. Comparison of characteristics and biocompatibility of green synthesized iron oxide nanoparticles with chemical synthesized nanoparticles. Environ Res 2021; 201: 111585.
[28] Sun J, Liu X, Huang J, Song L, Chen Z, Liu H, Li Y, Zhang Y and Gu N. Magnetic assembly-mediated enhancement of differentiation of mouse bone marrow cells cultured on magnetic colloidal assemblies. Sci Rep 2014; 4: 5125.
[29] Gao K, Wang P, Peng J, Xue J, Chen K, Song Y, Wang J, Li G, An X and Cao B. Regulation and function of runt-related transcription factors (RUNX1 and RUNX2) in goat granulosa cells. J Steroid Biochem Mol Biol 2018; 181: 98-108.
[30] Lu W, Shen Y, Xie A and Zhang W. Green synthesis and characterization of superparamagnetic Fe3O4 nanoparticles. J Magn Magn Mater 2010; 322: 1828-1833.
[31] Wei Y, Han B, Hu X, Lin Y, Wang X and Deng X. Synthesis of Fe3O4 nanoparticles and their magnetic properties. Procedia Engineering 2012; 27: 632-637.
[32] Dissanayake NM, Current KM and Obare SO. Mutagenic effects of iron oxide nanoparticles on biological cells. Int J Mol Sci 2015; 16: 23482-23516.
[33] Fan J, Schiemer T, Vaska A, Jahed V and Klavins K. Cell via cell viability assay changes cellular metabolic characteristics by intervening with glycolysis and pentose phosphate pathway. Chem Res Toxicol 2024; 37: 208-211.
[34] Liu Z, Wang W, Xia Y, Gao Y, Wang Z, Li M, Presicce GA, An L and Du F. Overcoming the H4K20me3 epigenetic barrier improves somatic cell nuclear transfer reprogramming efficiency in mice. Cell Prolif 2024; 57: e13519.
[35] Wang C, Wang J, Song F, Liu H, Sun L, Wei X, Zheng T, Qian H, Li X, Zhang W, Tang X and Liu P. Upregulation of histone H3 caused by CRYAA may contribute to the development of age-related cataract. Biocell 2023; 47: 143-154.
[36] Wang D, Shi Y, Wang Z, Zhang J, Wang L, Ma H, Shi S, Lian X, Huang H, Wang X and Lian C. Meiotic nuclear divisions 1 suppresses the proliferation and invasion of pancreatic cancer cells via regulating H2A.X variant histone. Biocell 2024; 48: 111-122.
[37] Alarifi S, Ali D, Alkahtani S and Alhader MS. Iron oxide nanoparticles induce oxidative stress, DNA damage, and caspase activation in the human breast cancer cell line. Biol Trace Elem Res 2014; 159: 416-424.
[38] Anttonen M, Pihlajoki M, Andersson N, Georges A, L'hôte D, Vattulainen S, Färkkilä A, Unkila-Kallio L, Veitia RA and Heikinheimo M. FOXL2, GATA4, and SMAD3 co-operatively modulate gene expression, cell viability and apoptosis in ovarian granulosa cell tumor cells. PLoS One 2014; 9: e85545.
[39] Viger RS, Guittot SM, Anttonen M, Wilson DB and Heikinheimo M. Role of the GATA family of transcription factors in endocrine development, function, and disease. Mol Endocrinol 2008; 22: 781-798.
[40] Hummitzsch K, Hatzirodos N, Irving-Rodgers HF, Hartanti MD, Perry VEA, Anderson RA and Rodgers RJ. Morphometric analyses and gene expression related to germ cells, gonadal ridge epithelial-like cells and granulosa cells during development of the bovine fetal ovary. PLoS One 2019; 14: e0214130.
[41] Naillat F. From ovarian development to folliculogenesis: essential networks sustaining the ovarian reserve. OBM Genetics 2022; 6: 153.
[42] Dewailly D, Robin G, Peigne M, Decanter C, Pigny P and Catteau-Jonard S. Interactions between androgens, FSH, anti-Müllerian hormone and estradiol during folliculogenesis in the human normal and polycystic ovary. Hum Reprod Update 2016; 22: 709-724.
[43] Liang A, Salzano A, D'Esposito M, Comin A, Montillo M, Yang L, Campanile G and Gasparrini B. Anti-Mullerian hormone (AMH) concentra-

tion in follicular fluid and mRNA expression of AMH receptor type II and LH receptor in granulosa cells as predictive markers of good buffalo (Bubalus bubalis) donors. Theriogenology 2016; 86: 963-970.
[44] Gao K, Chen Y, Wang P, Chang W, Cao B and Luo L. GATA4: regulation of expression and functions in goat granulosa cells. Domest Anim Endocrinol 2024; 89: 106859.
[45] Nicol B, Grimm SA, Gruzdev A, Scott GJ, Ray MK and Yao HH. Genome-wide identification of FOXL2 binding and characterization of FOXL2 feminizing action in the fetal gonads. Hum Mol Genet 2018; 27: 4273-4287.
[46] Elzaiat M, Todeschini AL, Caburet S and Veitia RA. The genetic make-up of ovarian development and function: the focus on the transcription factor FOXL2. Clin Genet 2017; 91: 173-182.
[47] Efimenko E, Padua MB, Manuylov NL, Fox SC, Morse DA and Tevosian SG. The transcription factor GATA4 is required for follicular development and normal ovarian function. Dev Biol 2013; 381: 144-158.
[48] Juan AH, Wang S, Ko KD, Zare H, Tsai PF, Feng X, Vivanco KO, Ascoli AM, Gutierrez-Cruz G, Krebs J, Sidoli S, Knight AL, Pedersen RA, Garcia BA, Casellas R, Zou J and Sartorelli V. Roles of H3K27me2 and H3K27me3 examined during fate specification of embryonic stem cells. Cell Rep 2017; 18: 297.
[49] Hayashi K and Yoshino T. Reconstitution of reproductive organ system that produces functional oocytes. Curr Opin Genet Dev 2022; 77: 101982.
[50] Cho YM, Kwon S, Pak YK, Seol HW, Choi YM, Park DJ, Park KS and Lee HK. Dynamic changes in mitochondrial biogenesis and antioxidant enzymes during the spontaneous differentiation of human embryonic stem cells. Biochem Biophys Res Commun 2006; 348: 1472-1478.
[51] Tyurin-Kuzmin PA, Molchanov AY, Chechekhin VI, Ivanova AM and Kulebyakin KY. Metabolic regulation of mammalian stem cell differentiation. Biochemistry (Mosc) 2020; 85: 264-278.
[52] Zhang N, Häring M, Wolf F, Großhans J and Kong D. Dynamics and functions of E-cadherin complexes in epithelial cell and tissue morphogenesis. Mar Life Sci Technol 2023; 5: 585-601.
[53] Zheng H, Ban Y, Wei F and Ma X. Regulation of interleukin-12 production in antigen-presenting cells. Adv Exp Med Biol 2016; 941: 117-138.
[54] Zhang Y, Marsboom G, Toth PT and Rehman J. Mitochondrial respiration regulates adipogenic differentiation of human mesenchymal stem cells. PLoS One 2013; 8: e77077.
[55] Hofmann AD, Beyer M, Krause-Buchholz U, Wobus M, Bornhäuser M and Rödel G. OXPHOS supercomplexes as a hallmark of the mitochondrial phenotype of adipogenic differentiated human MSCs. PLoS One 2012; 7: e35160.
[56] Shen YC, Shami AN, Moritz L, Larose H, Manske GL, Ma Q, Zheng X, Sukhwani M, Czerwinski M, Sultan C, Chen H, Gurczynski SJ, Spence JR, Orwig KE, Tallquist M, Li JZ and Hammoud SS. TCF21+ mesenchymal cells contribute to testis somatic cell development, homeostasis, and regeneration in mice. Nat Commun 2021; 12: 3876.
[57] An J, Zheng Y and Dann CT. Mesenchymal to epithelial transition mediated by CDH1 promotes spontaneous reprogramming of male germline stem cells to pluripotency. Stem Cell Reports 2017; 8: 446-459.
[58] Teng MW, Bowman EP, McElwee JJ, Smyth MJ, Casanova JL, Cooper AM and Cua DJ. IL-12 and IL-23 cytokines: from discovery to targeted therapies for immune-mediated inflammatory diseases. Nat Med 2015; 21: 719-729.
[59] Serrano MC, Pagani R, Manzano M, Comas JV and Portolés MT. Mitochondrial membrane potential and reactive oxygen species content of endothelial and smooth muscle cells cultured on poly (ε-caprolactone) films. Biomaterials 2006; 27: 4706-4714.
[60] Zorova LD, Popkov VA, Plotnikov EY, Silachev DN, Pevzner IB, Jankauskas SS, Babenko VA, Zorov SD, Balakireva AV, Juhaszova M, Sollott SJ and Zorov DB. Mitochondrial membrane potential. Anal Biochem 2018; 552: 50-59.
[61] O-Uchi J, Ryu SY, Jhun BS, Hurst S and Sheu SS. Mitochondrial ion channels/transporters as sensors and regulators of cellular redox signaling. Antioxid Redox Signal 2014; 21: 987-1006.
[62] Kim JH, Song SY, Park SG, Song SU, Xia Y and Sung JH. Primary involvement of NADPH oxidase 4 in hypoxia-induced generation of reactive oxygen species in adipose-derived stem cells. Stem Cells Dev 2012; 21: 2212-2221.
[63] Papa S, Martino PL, Capitanio G, Gaballo A, De Rasmo D, Signorile A and Petruzzella V. The oxidative phosphorylation system in mammalian mitochondria. Adv Exp Med Biol 2012; 942: 3-37.
[64] Sivandzade F, Bhalerao A and Cucullo L. Analysis of the mitochondrial membrane potential using the cationic JC-1 dye as a sensitive fluorescent probe. Bio Protoc 2019; 9: e3128.
[65] Botvin VV, Sukhinina EV, Fetisova AA, Wagner DV, Vedyashkina MY, Pryadko A and Surmenev RA. Changes in gene expression profile of normal human fibroblasts on P (VDF-TrFE) scaffolds highly doped with Fe_3O_4-CA nanoparticles under alternating magnetic field stimulation. European Polymer Journal 2024; 220: 113492.

[66] Magro-Lopez E and Muñoz-Fernández MÁ. The role of BMP signaling in female reproductive system development and function. Int J Mol Sci 2021; 22: 11927.
[67] Huang DM, Hsiao JK, Chen YC, Chien LY, Yao M, Chen YK, Ko BS, Hsu SC, Tai LA, Cheng HY, Wang SW, Yang CS and Chen YC. The promotion of human mesenchymal stem cell proliferation by superparamagnetic iron oxide nanoparticles. Biomaterials 2009; 30: 3645-3651.
[68] Bin S, Wang A, Guo W, Yu L and Feng P. Micro magnetic field produced by Fe3O4 nanoparticles in bone scaffold for enhancing cellular activity. Polymers (Basel) 2020; 12: 2045.
[69] Paliwal S and Sharma S. Functionalized magnetic nanoparticles for tissue engineering. Functionalized Magnetic Nanoparticles for Theranostic Applications 2024; 9: 283-318.
[70] Aquino-Martínez R, Artigas N, Gámez B, Rosa JL and Ventura F. Extracellular calcium promotes bone formation from bone marrow mesenchymal stem cells by amplifying the effects of BMP-2 on SMAD signalling. PLoS One 2017; 12: e0178158.
[71] Zhang Y, Zhang Y, Yang Z, Fan Y, Chen M, Zhao M, Dai B, Zheng L and Zhang D. Cytotoxicity effect of iron oxide (Fe3O4)/graphene oxide (GO) nanosheets in cultured HBE cells. Front Chem 2022; 10: 888033.
[72] Nejadali Chaleshtari S, Amini E, Baniasadi F, Tavana S and Ghalamboran M. Oocyte maturation, fertilization, and embryo development in vitro by green and chemical iron oxide nanoparticles: a comparative study. Sci Rep 2024; 14: 14157.
[73] Sun QY, Breitbart H and Schatten H. Role of the MAPK cascade in mammalian germ cells. Reprod Fertil Dev 1999; 11: 443-450.